Sate.llit e Radar lnt erferometry for Monitoring Ice-sheet Motion: Application to an Antarctic Ice Stream

Richard M, Goldstein, 1 Iermann Engelhardt, Barclay Kamb and Richard M. 1 rolich[1]

Abstract

As a new means of monitoring the flow velocities and grounding-line positions of ice streams, which are indicators of response of the Antarctic and Greenland ice sheets to climatic change or internal instability, the method of satellite radar interferometry (SRI) is here proposed and applied to the Rutford Ice Stream, Antarctica. The method uses phase comparison of the radar signal obtained for a pair of SAR images taken a few clays apart to plot an interferogram which directly displays relative ground motions that have occurred in the time interval between images. The detection limit is about 1.5 mm for vertical motions and about 4 mm for horizontal motions in the radar beam direction. in the Rutford Ice Stream, SRI velocities agree fairly well with earlier ground-truth data over a longitudinal interval of 29 km; the comparison suggests a secular decrease in velocity of about 2% from 1978-80 to 1992. Ungrounded ice is revealed by large (-2 m) vertical motions due to tidal uplift, and the grounding line can be mapped at a resolut ion of ca. 0,5 km from the SRI interferogram. The mapped configuration implies grounding line retreat of 1 to several km since 1980.

[1]R Goldstein, Jet Propulsion Laboratory, California Institute of Technology, Pasadena, CA 91 109; 11, Engelhardt and B. Kamb, Division of Geological and Planetary Sciences, California Institute of Technology, Pasadena, CA 91 12.S; R. Frolich, British Antarctic Survey, Cambridge, UK CB3 0ET.

Int reduction

The continuing current attention to the possible response of the polar ice sheets to global climatic change and/or internal instability ies (*1*, 2,.?) emphasizes the need for cont inued and if possible improved ice-sheet monitoring capabilities that can detect significant changes if and as they develop. Satellite monitoring of ice volume by precision altimetry of the ice-sheet surface is a promising technique that has just begun to yield results (4). Also needed is monitoring of ice flow velocities and the position of ice grounding lines, which relate closely to the possibility of icc-sheet disintegration: a marine-based ice sheet, like the West Antarctic ice sheet, whose base in its central part lies well below sca level, is subject to a type of instability in which grounding-line retreat leads to rapid outflow and icc-sheet collapse (5). For monitoring flow, the usefulness of satellite optical imaging has recently been shown by Bindschadler and Scambos (2). We here present a new satellite radar technique for determining ice flow velocity and also grounding line position, and wc show its application to a large, rapidly flowing Antarctic ice stream.

The Antarctic ice streams (6) arc fast-moving currents 30-80 km wide, and up to 500 km king, within the generally slow-moving ice sheet. They reach flow speeds of ~ 800 m a^{-1}, which arc ~ 100 times faster than the adjacent ice sheet (2,6). Because of the large ice flux that they carry, the ice streams make the major contribution ($\sim 90\%$) to outflow from the icc sheet; if they were to speed up and/or widen sufficientl y, they could become the immediate cause of ice- sheet collapse (5', 7). Monitoring the extent and motions of the ice streams is therefore of much importance in assessing ice sheet behavior. It can also contribute to the ongoing search for the physical mechanism of ice stream motion (6,6'), on the basis of which attempts to predict ice stream behavior arc being made (5').

The possibility of ice-stream monitoring by the new technique is illustrated with the Rutford Ice Stream, which is onc of the main outlets of the West Antarctic ice sheet, draining a large area around the Ellsworth Mountains and emptying into the head of the Ronne Ice Shelf (9), Because some ground and satellite data arc already available for it (9,10,11,12), the Rutford ICC Stream is an advantageous target for applying the new monitoring technique.

Satellite Radar Interferometry (SRI)

Satellite-bomc imaging synthetic-aperture radar (SAR), such as that current] y provided by satellite 111{ - 1 of the European Space Agency, presents the opportunity for measuring surface displacement fields interferometricall y by making use of the coherence of the radar beam in the following way (13). If two radar observations of the same scene are made from locations sufficiently close together, interference between the two resulting SAR images can bc obtained by comparing the phase of the synthesized signals making up the two images. As originally calculated from the radar return these images, called "single-look complex images" ("S1 .C images") by the European Space Agency, contain both amplitude anti phase information. Here wc call them complex images. In such an image the amplitude and phase at each pixel are given in the form of a complex number, from which the phase shift from image 1 to image 2 at each pixel can bc extracted. The result is displayed in an "interferogram" of the image pair (Fig. 1), which is an areal plot of tbc phase shift, spectrally color coded, as a function of position throughout the image.

At any point in the interferogram the phase shift is a measure of the line-of-sight component of displacement of the corresponding ground surface point in relation to the spacecraft from the time of onc image to the other. Half a wavelength of displacement (2,8 cm

in the example here) produces a phase shift of 360°. The actual zero of the phase shift is arbitrary, hence only displacements of one point relative to another in the field of view arc determined. If in traversing the fringe pattern in 1 ig. 1 wc pass from purple through blue and yellow to red and then to purple, we have passed through a change in phase shift by 360° in the direct ion that corresponds to the scattering points having moved 2.8 cm relative] y closer to the spacecraft from the time of the first image to the second.

SRI's resolution of displacements depends on the magnitude of the phase noise, which in Fig. 1 can be evaluated in areas of broad, widely spaced fringes, where the r.m. s. scatter in phase shif is found to be 17°. This corresponds to a line-of-sight displacement resolution of 1.3 mm. In comparison, the pixel size, which is what limits the resolution in non-interferometric imaging methods for measuring ground displacement (2,14), is ca. 65 m,

In order to obtain an SRI interferogram like Fig. 1 it is necessary to bring the two complex images into sufficiently good pixel-to-pixel registry by shifting one image relative to the other! This is done by means of a correlation algorithm (*15*). Once the registry position is established, a step of data averaging and condensation is introduced (16). Before calculating the interferogram a correction $\phi_1 - \phi_2$ is made to the phase shift at each pixel to remove a phase shift that arises not from ground motion but because the spacecraft was not at exactly the same position when the radar data for the two complex images were obtained. The geometry is shown in Fig. 2. The phase shift $\phi_2 - \phi_1$ (in radians) between scattered waves returning to the two spacecraft positions 1 and 2 from a given far-distant scattering point at an angle θ to the vertical is

$$\phi_2 - \phi_1 = \frac{4\pi}{\lambda}(V\cos\theta - H\sin\theta) \qquad (1)$$

where V and H are the vertical and horizontal components of spacecraft position 2 relative to position 1 as defined in Fig. 2 (17). The radar wavelength is λ (=-5.656 cm in the case of Fig. 1). The inclination angle θ runs from 19.9° to 26.6° in going from bottom to top in Fig. 1.

in principle, phase differences of the same type will arise from variations in elevation of the ground surface in the imaged area, but wc can show that they are negligible for interferograms of low-relief terrain (such as icc sheets and icc streams) obtained with a small separat ion between spacecraft positions 1 and 2 (small H and V). Fig. 3 shows the geometry. The change in phase shift $\Delta(\phi_2 - \phi_1)$ for waves scattered from, saY, a mountain top at elevation z, in relation to $\phi_2 - \phi_1$ for scattering from the datum level z =-0 at the same map-position, is obtainable from eqn. (1) by allowing θ to change by the amount $\Delta\theta = (z/\rho)\sin\theta$, where ρ is the slant range as shown in Fig. 3; AU can be treated as infinitesimal, because, for the conditions of 1 ig. 1, $z \lesssim 100$ m while $\rho \cong 850$ km (*18*). Wc calculate from eqn. (1) a change in phase shift of ≤ 0.50 for an elevation $z \leq 100$ m. This amounts to a change of less than 0,2% of one fringe, much smaller than the range of observed phase shifts (- 100 fringes) in Fig. 1.

Application of SRI to the Rutford Ice Stream

1 ig. 4 is a nearly conventional SAR image (*19*), 100 km by 49 km, showing a part of the 35-knl-wide Rutford Icc Stream centered at lat. 78043'S, long. 83 °0'W. North is approximately up, the azimuth of the radar line of sight (bottom to top in the figure) being 350.8°. in 1 ig. 4 the ice stream extends from top to lower right (roughly north to south) through the central part of the image, and the bright bands to the left and right arc its marginal

shear zones, where radar reflections from numerous ice-air interfaces in these crevassed zones give a bright radar return. A similar high radar reflectivity from crevassed marginal shear zones is observed for ice streams of the Siple Coast region (20). At the lower left in Fig. 4, the Minnesota Glacier enters the ice stream from the west, and at the upper left the irregular bright area west of the ice stream is the Flowers Hills, on the east side of the Ellsworth Mountains. Typical "flow bands" -- highly elongate surface ridges and troughs parallel to ice flow -- are visible on the Minnesota Glacier and in parts of the marginal shear zones. These features are also seen in satellite optical images of the ice stream (9, 10,21).

The SAR image in Fig. 4 has been amplitude extracted from one of four complex images of this part of the Rutford Ice Stream taken by ERS-1 from nearly coincident orbits at intervals of several days. Pairs of these images were phase compared in search of the SRI type of interference as described in the last section, and one suitable pair was found, giving the interferogram in Fig. 1, obtained by the procedure described in the last section. Upon the color-modulated interferogram in Fig. 1 is superimposed in shades-of-gray the SAR image in Fig. 4, so that the two can be directly compared.

Fig. 5 is a black-and-white version of the interferogram (Fig. 1) showing the fringe pattern and omitting the SAR image (except as noted in the figure caption). in Fig. 5 the x and y coordinates are at the same scale (as shown by the marginal ticks), which eliminates the image distortion in Figs. 1 and 4.

The flow direction of the ice stream, which is approximately parallel to its margins, is roughly south and roughly aligned with the top-to-bottom direction in Figs. 1, 4 and 5, that is, roughly along the horizontal projection of the reverse line-of-sight direction toward the spacecraft. The angle between the actual ice-stream flow direction and the horizontally projected

reverse line of sight is generally CIOSC to 24°. The fringe pattern in Fig. 1 thus gives an immediate rough picture of the variation of flow velocity laterally and longitudinally over the icc stream surface, except for complications duc to unground ing as discussed later. As wc traverse the image and pass from purple through blue and yellow to red and then to purple in the fringe pattern, the line-of-sight component of velocity toward the spacecraft increases by 0.47 cm/d (2.8 cm in 6.0 days). The corresponding increase in flow velocity, assumed to bc horizontal and at an azimuthal angle $\psi \cong 2.40$ relative to the horizontally projected reverse line of sight, is 0.47 $(\sin\theta \cos\psi)^{-1}$ cm/d or about 1.2 cm/d (for $\theta \approx 25°$). (The velocities arc of course time averages over the 6-day period bet wccn images.)

The main overall features of the interferogram in Fig. 1 arc the generally broad transverse fringes in the central part of the icc stream, giving way to narrow, closely spaced, longitudinal fringes in the marginal shear 7.ones. "l'his corresponds to low Jlow-velocity gradients in the central zone, going over to high shear rates in the marginal z.ones. The flow velocity decreases outward toward the margins as shown by the succession of fringe colors, and the marginal shear terminates very abruptly at the outer edge of the marginal zones, except where the Minnesota Glacier enters the icc stream. This flow-velocit y pattern is typical of ice streams (2,6,10). Very striking and atypical, however, is the large increase in apparent flow velocity in the longitudinal interval from $(x,y) = (25,25)$ to $(x,y) = (38,25)$. (Coordinates are given in km in the coordinate system of Figs. 1, 4, and 5.) As explained below, this large effect is due to ungrounding of the icc stream near $(x,y) = (25,25)$. outside the ice stream the fringes arc very broad and widely spaced, which is compatible with small icc motions there. An exception is a pattern of fringes duc to the flow of the Minnesota Glacier.

Although the fringes themselves give only relative velocity across the ice surface, "absolute" velocit ics can be obtained by counting fringes from an image point outside the ice stream where the surface velocity can reasonably be assumed to be essentially 0. Wc make this assumption for a point at $(x,y) = (34,5)$, just southwest of the southern prong of the 1 'lowers Hills (22). Fringes can be counted from that point along a path running generally southward outside the icc stream, into the Minnesota Glacier in the lower left corner of Fig. 1, and from there eastward into the marginal shear zone. in Fig.· 1 the fringes secm to disappear in the marginal shear zones, suggest ing that the radar returns from these zones were incoherent. However, an enlargement of part of the interferogram, given in Fig. 6, shows that in the marginal area near the Minnesota Glacier, where the marginal fringes arc somewhat wider than elsewhere, coherence is not lost and extremely fine fringes can be detected and counted clear through the zone. From the assumed zero point Up to the fringe peak at $(x,z) = (38,25)$ a total of 147 fringes is counted. From the peak the fringes can be counted downward by two different paths, roughly along y = 20 km and y== 30 km in Fig. 1, to points in the grounded zone: at $(x,y) = (2.0,2,5)$ the downward count is 60 fringes by both paths, giving a net upward fringe count of 147--60=87 relative to the zero. The corresponding flow velocity at (x,y)=(12,25) is 87 X1.2 cm d-l== 381 m a^{-1}. (In principle there is a correction duc to the fact that θ varies along the traverse where the fringes were counted, but the correction proves to be small,)

An alternative method for identifying the Z.cro-velocity fringe makes usc of the curving flow of the Minnesota Glacier that is indicated by the curving flow bands in Fig. 4: where the curving bands have a "horizontal" tangent in Fig. 4, the flow is perpendicular to the radar beam anti the line-of-sight velocit y component is O. This criterion, applied to the flow bands and

fringes near (x,-y) =(69,21), selects a zero fringe that differs by about 3/4 of a fringe from the one chosen at $(x,y) = (34, 5)$.

By fringe counting as described above (with correction for variation of 0), the apparent flow velocity was determined along a near-centerline longitudinal profile starling at $(x,y) = (O, 14)$ and shown by the longitudinal line in Fig. 5. The results are given in Fig. 7 (solid and dot-dash curve), where they are compared with ground-based velocity measurements along the same profile (dashed and dotted curves) (*10*). in Fig. 7 the velocity data are plotted against the longitudinal centerline coordinate (cc, in km) used by (*10*); cc is 100 at the upstream end of the longitudinal profile in Fig. 7. From cc 100 to about 124 the agreement between the SRI velocity measurements and the ground truth is rather good, although the SRI velocities are generally low by about 10 m a^{-1} (2%) in relation to the ground-based velocities, which were measured in 1978-80 and 1984-86. This discrepancy could arise if the ice motion at the assumed fringe zero point was not zero, or it might be due to a secular decrease in flow velocities from the epoch of the ground surveys to 1992. The small increase in velocity from 1978-80 to 1984-86 indicated by the ground data is statistically of only marginal significance according to (*10*).

A velocity profile across the grounded ice stream at $x = O$, based on the fringe pattern in Fig. 1, is given in Fig. 8 and compared with ground-based velocities along nearby transverse line D of (*10*), at cc 100. The wide central band of nearly constant velocity is sharply distinguished from the narrow marginal zones of high shear, about 4 km wide. A similar pattern is shown by Ice Stream E except that its central band contains pronounced velocity variations, which appear to be related to basal topography (2). Fig. 8 suggests, like Fig. 7, that there has been a secular decrease in flow velocity by about 10 m y^{-1} from 1978-80 to 1992.

Tidal Motion and Grounding **Line**

Downstream from cc 128 in 1 ig. 7 the apparent horizontal velocity determined from SRI as described above shows a large upswing to a much higher level that continues to the end of the centerline longitudinal profile at cc 145, Fig. 1 shows that the high apparent velocities extend continuously with modest decrease along a broad central band from the peak at $(x,y) = (38,25)$ for some 50 km southward and somewhat eastward to the edge of the image and doubtless beyond. These high apparent velocities arc clue to vertical motions where the ice stream is afloat and moves vertically with the ocean tide. The tidal motions contribute strongly to the line-of-sight displacements detected by SRI, because the line of sight is inclined only $\theta \approx 23°$ from vertical. I lence when tidal motions are involved the SRI results cannot be interpreted in terms of a horizontal ice flow velocity alone. For this reason the part of the SRI curve beyond cc 128 in Fig. 7 is shown with a dash-dot line to distinguish it from the curve upstream from cc 128 where the icc is grounded and the horizontal velocity interpretation is most] y valid, (The vertical component of flow velocity for the grounded ice stream has a generall y negligible effect except as noted in the next sect ion.)

The heavy dashed curve in Fig. 9 is the grounding line as mapped on the ground (*12*), and the heavy solid curve, drawn from Fig. 5, is the sharp edge of the ca,-7-lm~-wide "tongue" of broad, widely spaced fringes that runs southward from about $x = 6$ to a tip at about $(x,y) = (22,24)$. outside of this "tongue" the fringe count rises rapidly, corresponding to the upswing of the dash-dot curve beyond cc 128 in 1 ig. 7, The fairly good agreement between the dashed and solid curves in 1 ig. 9 supports interpretat ion of the edge of the "tongue" as the grounding line.

in order to evaluate tidal motion as the cause of the fringe pattern outside of the "tongue" wc interpret the SRI velocity curve in Fig. 7 as follows. Wc subtract from the solid and dash-clot curve in Fig. 7 a horizontal velocity component given by the ground-based measurements (dashed curve) reduced everywhere by 8 m a^{-1} so as to match generally the SRI results for the grounded icc stream (solid curve). The remainder (after the subtraction) is reconverted to fringe counts and then reprojected to the equivalent vertical displacement that would produce these fringe counts. The result is plotted as the solid curve in Fig. 10. It shows that a tidal uplift of about 2 m between the first and second radar observations would account for the magnitude of the rise in fringe count beyond the grounding line. Since the observed tidal amplitudes are of order 2 or 3 m, a tidal uplift of this magnitude between the two observations is quite possible if the phasing of the tides was right. This can be chcckcd because the Fourier components for the observed tide near the ungrounded Rut ford Icc Stream have been evaluated (12,24). On this basis, C.S.M. Doake (personal communication) has kindly calculated by Fourier synthesis the tidal level at the two observation times and finds that between the first and second observations there was a tidal rise of 2.1 ±0.2 m, which corresponds well with the peak of the solid curve in Fig. 10.

The distance scale of about 10 km over which the tidal uplift increases from O at the grounding line to 2 m at the uplift peak in Fig. 10 is reasonable, as is seen by calculating from the theory of ice shelf tidal flexure the expected shape of the uplift curve. According to the standard bending-elastic-beam model of tidal flexure (24) the tidal uplift curve Az(x) for the ungrounded part of the icc stream has the form

$$\Delta z(x) = \Delta z_{\infty}\left[1 - e^{-\beta x}\sqrt{2}\ \sin(\beta x + \frac{\pi}{4})\right]. \qquad (2.)$$

Here $\Delta z(x)$ is the change in elevation of the ice surface at x when the far-field tidal rise from observation 1 to observation 2 is Δz_{∞}; x is distance downstream from the grounding line, and β is a parameter that depends on the ice thickness and elastic modulus. The clotted curve in Fig. 10 is calculated from eqn. (5) with $\Delta z_{\infty} = 2.07$ m and with $\beta = 0.26$ km^{-1}, close to the preferred mode] value of Smith (24) for the Rut ford Icc Stream ($\beta = 0.25$ km^{-1}). The origin for x, where Az= O, is taken at cc 128 (2.5), The good agreement of the observed and calculated curves in Fig. 10 supports the tidal uplift interpretation (*26*).

The progressive decrease in fringe count along the central band of broad fringes that extends downstream from the fringe peak at $(x,y) = (38, 25)$ is probably due mainly to downstream decrease in the flow velocity of the ice stream, cent inuing downstream the trend seen over the interval cc 114-146 in the ground-based velocities (Fig. 7, dashed curve). Interpreted in this way, the fringe pattern indicates a flow velocity of about 255 m a^{-1} where the central band exits from the image at $(x,y) = 70,50$.

Where the Minnesota Glacier enters the icc stream, near $(x,y) = (75, 25)$ (Fig. 1), the closely-spamd fringes in the marginal shear zone of the icc stream are "pushed" inward into the icc stream. Part of this feature is seen in enlarged detail in Fig. 6, The "push-in" extends into the central band of broad fringes near $(x,y) = (64,36)$. This feature reflects some combination of reduced flow velocity and/or reduced tidal uplift in the area where the glacier enters the ice stream. I tither or both effects could result from grounding or partial grounding of the icc stream in this area, duc to ice thickening that results from inflow of the tributary glacier. Doake et al. (9) have identified the area of the "push-in" as onc of a number of locally grounded areas

located by radio-echo sounding downstream from the main grounding line. The curious "IM3I1ow" in the fringe pattern near $(x,y) = (44,38)$ appears to correspond to the upstream tip of another such grounded area.

The comparison in Fig. 9 between the grounding line as indicated by Fig. 1 (1992 data) and the earlier (1980) ground-based determination (*12*) suggests some retreat of the grounding line between 1980 and 1992, perhaps as much as a kilometer near the tip of the "tongue," and possibly several kilometers on the western side of Fig. 9. However, such a conclusion is at this stage made somewhat uncertain by possible uncertainty in registration between the SAR image and the ground-based map (23), and also by tbc problematical aspects of the ground-based determination of the grounding linc, as indicated by comparing the results of (*12*) and (24).

Vertical flow component of grounded ice

From cc 124 to 129 in Fig. 7 the SR1 velocity (solid curve) traces out a small peak at cc 126 followed by a small minimum at cc 128, which are not seen in the grouncl-based (dashed) curve. We interpret thcm as due to mall vertical motions of the grounded ice, which arc represented by the corresponding small peak and minimum in Fig. 10. These features approximately bracket an ice-surface hump that is visible near lat. 78029.7 'S, long. 8305' W in Landsat optical images (9,10,21). Ice flow over the hump (27) results in a relatively upward vertical component of ice motion on the upstream side and a relatively downward component on the downstream side, which produces the peak followed by a minimum at cc 126 and 128 in Fig. 10. From the height and horizontal dimension of the hump (20 m and 2 km) and the horizontal velocity (390 m a^{-1}) we can estimate the expected difference in vertical velocity between the

peak and the minimum; it is *0.2* meters in *6* clays, in rough agreement with the difference of 0.15 meters (in 6 days) between the observed uplift values of the peak and minimum in Fig. 10.

Fig. 1 shows that the peak and minimum bracket a prominent bright patch seen in Fig. 4 near the center of the ice stream. Like the marginal shear zones, the brightness of this patch in the SAR image is probably due to crevassing, which appears to be caused by flow over the hump.

Comparison of SRI and imaging

The satellite sequential imaging method, which has been developed for ice-stream flow velocity monitoring by Bindschadler and Scambos (2), is limited by pixel-size displacement resolution (ea. 30 m) (28), whereas the resolution of SRI is not limited by the pixel size and is very much finer, ca. 1 cm for horizontal displacements, A compensating limitation for SRI is that interference cannot be obtained from a pair of complex images taken more than a few days apart in time, because ongoing changes in the ice/snow surface at the radar wavelength scale ultimately destroy the detailed phase coherence between the two images upon which the interference depends. Images taken 2 years apart were used to obtain ice flow velocities by the sequent ial imaging method (2), whereas for SRI we here usc a pair of complex images taken 6 days apart. in the determination of flow velocities the factor $\sim 10^3$ in improved displacement resolution by SRI is thus offset by a factor -10-2 in available elapsed time for the displacement measurement. 1 lowever, the ability of SRI to get results in a much shorter time and without interference from darkness or cloud cover (which bedevils optical imaging) is decidedly advantageous. Also, SR1 does not depend upon the presence and resolution of pixel-scale surface features such as crevasses or snow dunes, as the imaging method dots,

Both SRI and the sequential imaging method are limited to detecting only relative ice motions unless within the image there are fixed bedrock points *(22)* or ice features that remain fixed with respect to bedrock. Bindschadler and Scambos (2) found that broad, gentle topographic undulations, made visible in optical (Landsat) images by faint sun shadowing or scattering-angle effects, remained fixed in position relative to bedrock below and could be used as a "surrogate bedrock reference" to obtain absolute flow velocities by sequential imaging. Surprisingly they report ±1 pixel (528 m) precision in locating these undulations in the images, even though the undulation wavelengths are much longer, >1 km (2). Some of the undulations appear similar to the hump on Rutford Ice Stream noted in the last section. However, for SRI there is no counterpart to the undulation bedrock reference. To obtain an approximation to absolute flow velocities in an ice stream by SRI one is therefore dependent upon assuming a reference point of O or small velocity outside the ice stream (29). This approach is also dependent on resolution of the closely spaced fringes clear through the marginal shear zone, which is difficult, as noted earlier. This approach can be used to monitor the ice streams for substantial changes of flow without danger of more than a small error from change in ice motion at the reference point because the flow velocities outside the ice streams are comparatively so small (2,6).

The limitation of SRI to detection of motion only in the line-of-sight direction of the radar beam means that only one component of the horizontal flow can be measured from an image pair, whereas the imaging method obtains the full horizontal velocity. The limitation could be overcome by a second set of SRI data with a roughly perpendicular line of sight, but this may or may not be obtainable, depending on the orbital inclination of the satellite and the latitude of the target ice stream. However, because the ice stream motions and the motion

sensitivity of SRI are so large, the measurement of one component within, say, 60° of the flow direct ion would bc sufficient for monitoring ice-stream flow changes.

SRI is sensitive to vertical motions, whereas the imaging method is not. Thus SRI can detect tidal motions and thereby locate grounding lines, as shown above, while imaging cannot. SRI monitoring of changes in grounding-line position from one interferogram to another is probably not limited by the accuracy of grounding-line location in the fringe pattern but rather by the registry of the interferograms in relation to fixed bedrock. Analogous] y to what can be done with opt ical images as noted above (2), for interferogram registry a "surrogate bedrock reference" may be provided by features in the SAR image such as the bright patch mentioned in the last section or by the small maxima and minima in vertical motion associated with flow over humps in the ice surface topography, an example of which was discussed in the last section,

Conclusions

Satellite radar interferometry (SRI) is capable of observing the horizontal flow velocities in grounded ice sheets and ice streams at a resolution level of about 1 m a^{-1}, which is in the lower part of the range of typical ice-sheet motions ($\lesssim$ 10 m a^{-1}) and represents a very sensitive detection level for the flow of Antarctic ice streams (-400 m a^{-1}). Although only relative velocity is directly measured, absolute velocity can be obtained if the relative velocities arc referenced to a slowl y moving point outside the ice stream, This allows ongoing monitoring of the ice streams for changes in flow at roughly the 2% level, the main uncertainty being not in the SRI measurement but in the possible change in motion of the slow moving reference point. Results arc obtainable in about a week (not counting data distribution and processing time). Grounding line position can bc monitored to an accuracy of about 0.5 km, if successive SRI

interferograms are coregistered by means of features in the SAR images or in the fringe patterns that can be recognized to stay fixed in relation to bedrock, a coregistration technique analogous for radar to one that works for optical images (2). The SR1 method is a significant addition to the satellite sequential imaging method (2) in monitoring the ice streams for current changes that may result from climatic change or internal instability. Changes in the Rutford Ice Stream are already detected, albeit marginally, by comparing SRI results with earlier ground-based observations.

References and notes

1. J. Oerlemans, C.J. van der Veen, Eds., *Ice Sheets and Climate* (Reidel, Dordrecht 1984); National Research Council Ad Hoc Committee on the Relation between Land Ice and Sea Level, *Glaciers, Ice Sheets, and Sea Level: Effect of a CO_2-Induced Climatic Change* (National Academy Press, Washington, DC, 1985); R.B. Alley, *Episodes* **13**, 231 (1990); R.A. Warrick, J. Oerlemans, in *Climate Change: The IPCC Scientific Assessment,* J.T. Houghton, G.J. Jenkins, J.J. Ephraums, Eds. (Cambridge Univ. Press, 1990); M.F. Meier, *Nature* 343, 115 (1990); R.B. Alley, I.M. Whillans, Science 254, 959 (1991); C.S. Lingle, D.H. Schilling, J.J. Fastook, W.S.B. Paterson, T.J. Brown, *J, Geophys. Res.* 96, 6849 (1991); T.J. Hughes, *Palaeogeogr., Palaeoclimatol, Palaeoecol.* (Global and Planetary Change Section) 97, 203 (1992); D. Sugden, *Nature* 359, 775 (1992); S.S, Jacobs, *Nature* 360, 29 (1992).

2. R.A. Bindschadler, T.A. Scambos, *Science* 252, 242 (1991).

3. D.R. MacAyeal, *Nature 3S9, 29* (1992).

4. H.J. Zwally, A.C. Brenner, J.A. Major, R.A. Bindschadler, J.G. Marsh, *Science* 246, 1587 (1989); C.J. van der Veen, *Rev. Geophys.* 29, 433 (1991).

5. R.H. Thomas, *J. Glaciol. 24, 167 (1979).*

6. C.R. Bentley, *J. Geophys. Res. 92, 8843 (1987); 1.M.* Whillans, J. Bolzan, S. Shabtaie, *J. Geophys. Res. 92, 8895 (1 987).*

7. T.J. Hughes, *Rev. Geophys. Space Phys.* 1S, *44 (1977);* J. Weertman, G.E. Birchfield, *Ann. Glaciol.* **3**, 316 *(1982);* C.S. Lingle, T.J. Brown, In *Dynamics of the West Antarctic Ice Shed,* C.J. van der Veen, J. Oerlemans, Eds. (D. Reidel, Norwell, MA 1987) p.279; C.J. van der Veen, *ibid.,* p.8.

8. R.B. Alley, D.D. Blankenship, S.T. Rooney, C.R. Bentley, *J. Glaciol.* **35**, 130 *(1989);* 11. Engelhardt, N. Humphrey, B. Kamb, M. Fahnestock, Science 248, 57 (1990); R.B. Alley, *Episodes* **13**, *235 (1990);* B. Kamb, *J. Geophys. Res. 96, 16,585 (1991).*

9. C.S.M. Doake, R.M. Frolich, D.R. Mantripp, A.M. Smith, D.G. Vaughan, *J. Geophys. Res. 92,* 8951 *(1987).*

10. R.M. Frolich, D.G. Vaughan, C.S.M. Doake, *Ann. Glaciol.* **12**, *51,* especially Figs. *6* and *7 (1989).*

11. *S.N.* Stephenson, C.S.M. Doake, *Ann. Glaciol.* **3**, *295* (1982).

12. *S.N.* Stephenson, *Ann. Glaciol. 5, 165 (1984).*

13. *The* basic method, but directed toward the detection of vertical displacements, was introduced by A .K. Gabriel, R.M. Goldstein, 11 .A. Zebker, *J. Geophys. Res.* 94, 9183 (1989); a version of the method for measuring horizontal flow in ocean currents was described by R.M. Goldstein, H.A. Zebker, *Nature 328, 707 (1987)* ant] by R.M. Goldstein, 'l'.l'. Barnett, H .A. Zebker, *Science* 246, 1282 (1989).

14. R.E. Crippen, *Episodes 15,* 56 (1992).

15. We start from an approximate registry based on spacecraft orbit and image parameters. For a given positioning of the first image in relation to the second, the phase at each pixel in a test square (16x 16) in the first image is compared with the phase at the corresponding pixel in the second, and the phase difference is coherently averaged over the square by means of a discrete two dimensional Fourier transform, giving a correlation measure. This procedure is repeated with the second image shifted by a certain number of pixels relative to the first; 81 relative shifts, corresponding to shifts to pixels in a 9X9 square, are tested in this way. If a distinct maximum in the correlation measure is found within the 9X9 square, the maximum point is the local registry position for the two images. The procedure is repeated for a number of 16×16 squares distributed across the image. in calculating the interferograms the registry position is taken to vary across the image in accordance with the smoothed results of the above registry search, allowing also for a discontinuity in registry position between the ice stream and the area outside of the ice stream. The variation is slight, 1 pixel spacing or less, but it has a significant effect on fringe quality.

16, Each original high-resolution complex image data set supplied by the European Space Agency consists of a 2500 x 12288 array of complex numbersgiving pixel amplitude and phase, 2500 rows in the range direction (bottom to top in Fig. 1) and 12288 in the cross-range direction (right to left). We average the pixel complex numbers by groups of 4 in the range direction ancl by groups of 12 in the cross-range direction, condensing the data set to a 62.5X 102.4 array, in which phase noise has been greatly decreased by the averaging. Each original data set processed as just described covers half of the complete

radar image, either the near-range or far-range half; the near and far halves are combined to form the full interferogram. For the result in Fig. 1, the pixel size on the ground is 80 m (on average) in range by 48 m in cross range, and the dimensions of the area imaged is 100 km in range by 49 km in cross range.

17. If the spacecraft orbits on which positions 1 and 2 lie are not exactly parallel (as is the case for Fig. 1), *H* and *V will* vary slightly across the image (right to left in Fig. 1) and the correction $\phi_1 - \phi_2$ varies accordingly,

18. Fig. 3 is for a "flat earth" approximation in which θ at the scattering site is the same as θ at the spacecraft position.

19. The SAR image in Fig. 4 is unconventional to the extent that in the procedure for averaging over adjacent pixels to suppress noise, as in note (16), the complex-image values were averaged before extracting the signal amplitude, whereas for a conventional SAR image the individual pixel amplitudes are first extracted and then averaged. The former procedure is better for bringing out weak details in the image.

20. K. R. Rose, *J. Glaciol.* 24 (90), 63 (1 979).

21. U. S. Geological Survey and British Antarctic Survey, *Rutford Ice Stream, Antarctica*, Satellite Image Map (1 :250,000) (1989).

22. The Flowers Hills are bedrock (with a discontinuous veneer of snow and ice) and should in principle provide reference points of O velocity, but their fringe pattern is so complicated that we cannot pick a O-velocity fringe there. This may imply a general limitation on using bedrock points such as nunataks to provide the reference for absolute velocities in the SRI method.

23. The solid and clashed curves in Fig. 9 arc positioned in relation to the indicated latitude and longitude lines as follows. For the solid curve, the interferogram in Fig. 5 was resealed to the scale of the satellite image map (*21*) on the basis of image parameters furnished by ESA, and a transparency of the image was registered to the map by registering the icc stream margins and the Hewers 1 Hills; the latitude and longitude lines from the map were then transferred to the image, on which the grounding line was drawn on the basis of the fringe pat [cm. For the clashed curve, the longitude and latitude lines in 1 'ig. 2 of (*12*) were transferred to Fig. 5 of (*12*) by using as a reference the frame of Fig. 5 that is shown in Fig. 2 of (*12*); after resealing, the grounding line in Fig. 5 of (*12*) could be positioned in relation to the solid curve in our Fig. 9 by registering the latitude and longitude lines.

24. A.M. Smith, *J. Glaciol.* 37, 51 (1991).

25, This is the appropriate choice of origin because $d\Delta z/dx = 0$ on the observed (solid) curve there, which is what the model (19) assumes. Because the model has $\Delta z = 0$ there, the uplift values on the calculated (dotted) curve arc obtained by adding $\Delta z(x)$ from eqn. (5) to the observed uplift value (–0.05 m) at cc 128.

26. Very close agreement is not cxpcctcd, because the model assumes a two-dimensional flexure geometry whereas the actual geometry is decidedly three-dimensional, with the "tongue" of grounded icc surrounded on three sides by tidal uplift (Fig. 1).

27. Strictly, instead of "flow over the hump" wc should say "flow over bedrock features that are responsible for the hump" or "flow following the curved surface of the hump."

28. Bindschadler and Scambos (2) report achieving sub-pixel resolution by a cross-correlation method, and Crippen (*14*) cites examples of O. OS-pixel precision in sequential imaging applied to tectonic deformation, but these resolutions are still far inferior to SRI.

29. This assumption can be avoided where flow transverse to the line of sight occurs within the image, as in the Minnesota Glacier discussed earlier.

The research described in this paper was carried out, in part, by the Jet Propulsion Laboratory, California Institute of Technology, under a contract with the National Aeronautics and Space Administration.

Figure Captions

Fig. 1. Radar interferogram of an area that includes a portion of the Rutford Ice Stream, Antarctica, produced by Satellite Radar Interferometry (SRI) as described in the text. The radar line-of-sight direction ("range direction") is up. The color fringes show the phase shift of the radar return, which is due to movement of the ice surface relative to the spacecraft during the 6-day period between two radar observations of the same scene. Phase shift modulo 360° is coded in 16 spectral color steps covering the range from 0° to 360°. The distance scales in the range direction (up-down) and cross-range direction (left -right) are different, as shown by the ticks along the margins indicating x and y coordinates in km. Superimposed on the phase-shift interferogram is a radar amplitude image (conventional SAR image) of the same area, in shades of gray, For further information see Figs. 4 and 5.

Fig. 2. Interference geometry for radar waves emanating from and returning to the radar satellite at two nearby positions, labeled 1 and 2. Positions 1 and 2 are occupied momentarily by the satellite at different times and lie on different local orbital paths, which are perpendicular to the plane of the paper. The distance between positions 1 and 2 is designated in terms of its horizontal component H and vertical component V, The outgoing and returning (scattered) radar waves transmitted and received at each of the two spacecraft positions are represented by outgoing/returning rays inclined at angle O to the vertical. The scattering point on the ground is far away (-850 km), so the rays are drawn parallel. If the scattering point remains fixed in position, the plane wave returning to position 1 will lead the wave returning to position 2 by

twice the distance s indicated in the drawing, hence wave 2 is phase shifted relative to wave 1 by $\phi_2 - \phi_1 = (2s/\lambda) \cdot 360°$.

Fig. 3. Geometry of the ground-elevation effect on SRI. The plane of the diagram is the same as Fig. 4, but the scale here is much compressed: the elevation of the spacecraft is ~800 km, whereas H and V in Fig. 4 are ~10 m. Hence 1 and 2 are shown here as a single point, labeled "spacecraft positions 1 and 2." The radar ray path for scattering from the top of a peak (point T) at elevation z above the datum is compared with the ray path that would be followed if there were no mountain and the scattering were from a point B on the datum directly below T. Since z is small compared to the slant range ρ (~850 km), the angle $\Delta\theta$ can be treated as infinitesimal.

Fig. 4. Conventional SAR image (*19*) of the same area as Fig. 1. Brighter areas represent greater strength of the radar return. The Rutford Ice Stream is the wide dark band with bright margins that enters the frame at the top, toward the left side, and extends southeastward, exiting out the lower half of the east side of the frame.

Fig. 5. Fringe pattern from the interferogram of Fig. 1. Pixels for which the phase shift is in the range 2250-2360 (color red in Fig. 1) are here marked with a black dot. The image area is the same as in Fig. 1, except for omission here of an 11-km-wide strip at the bottom. The x,y coordinate system, in km, shows the dimensional scale and is used in the text to locate points in the image. The image distortion in Fig. 1 due to nonlinearity of the x scale and inequality of the x and y scales is here removed. Latitude and longitude are shown by labeled

crosses. The longitudinal line running somewhat east of south from $(x,y) = (0, 14)$ is a profile along which flow velocity and tidal uplift data are given in Figs. 7 and 10. Within the area of the Flowers 1 Hills (upper left, west of the ice stream), radar amplitude information is included in order to improve the visibility of the hills for registry with other images such as Landsat.

Fig. 6. Enlargement of a portion of Fig. 1 in the area where the Minnesota Glacier feeds into the Rutford Ice Stream. The radar amplitude (SAR) image is here omitted, so that only the phase shift between the two complex images is portrayed. The enlarged area is bounded by x and y coordinates as indicated, For greater spatial resolution of the fringes, the data averaging procedure (*16*) is here modified by averaging over only 4 pixels in the cross-range direction and eliminating averaging in the range direction, giving a pixel size 16 m **X** 20 m.

Fig. 7. ICC stream flow velocities along the longitudinal profile marked in Fig. S. The abscissa is the longitudinal centerline coordinate (cc, in km) of (10), with origin 100 km upstream from the start of the profile shown here. cc 100 corresponds to $x = 0$ in Fig. 5, The curve labeled SRI is obtained from the SRI data in Fig. 1 under the assumption that the phase shift results from horizontal mot ion in the direction of ice-stream flow (see text). This assumption holds for most of the solid part of the curve, but not for the dash-dot part, which is greatly affected by vertical (tidal) motions and therefore represents unreal horizontal velocities. The dashed and dotted curves arc ground-based velocity measurements made in 1978-80 and 1984-86 respectively (*10*).

Fig. 8. Transverse profile of flow velocity at $x = 0$ from SRI (solid curve) and from ground observations (dashed curve) on transverse profile D of (*10*), which is a transverse line passing approximately through $(x,y) = (3,7)$. Because the transverse direction is 24° askew to the $x = O$ profile line, the transverse coordinate for plotting the profile-D velocities has been scale up by (cos 240, -1 so that the edges of the icc stream in the two profiles match, at y== 1 and y= 32. In the marginal shear zones, where the fringes are too narrow to resolve, the SRI velocity curve is interpolated by dash-dot lines to velocity values just at the margin, where a near-zero velocity is assumed, A similar interpolation would apply to the ground-based measurements, which do not extend into the marginal shear zones.

Fig. 9. Map of the grounding line of the Rutford Ice Stream: solid curve: grounding line as obtained from SR1 in 1992 (Figs. 1 and 5); dashed curve: grounding line as found from ground observations in 1980 (12,23). The area of currently grounded ice is lightly patterned, and the marginal shear zones arc more heavily path.med. Ice flow is from top to bottom.

Fig. 10, Tidal uplift of the Rutford Ice Stream. The solid curve is the uplift observed by SRI (Fig. 1) on the basis described in the text. The tidal uplift starts at the grounding line at cc 128 and grows rapidly downstream. The dotted line is the theoretical tidal uplift calculated from eqn. (2) with $\Delta z_\infty = 2.07$ m, $\beta = 0.26$ km^{-1}, and with $x = O$ at cc 128, The small observed peak at cc 126 and trough at cc 128 are uplift features related to icc flow over a topographic hump as discussed in the text.

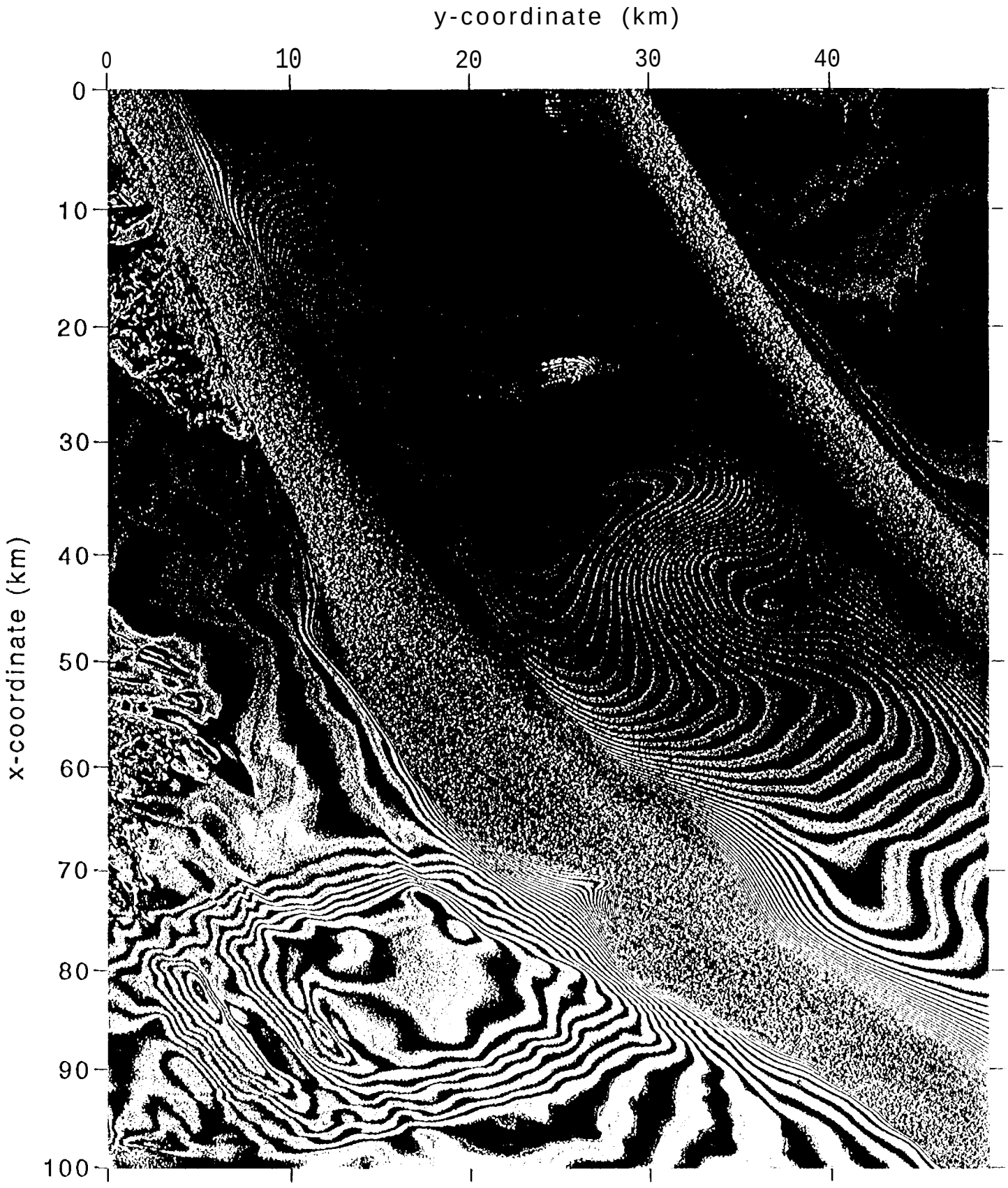

FIG. 1
Goldstein et al.

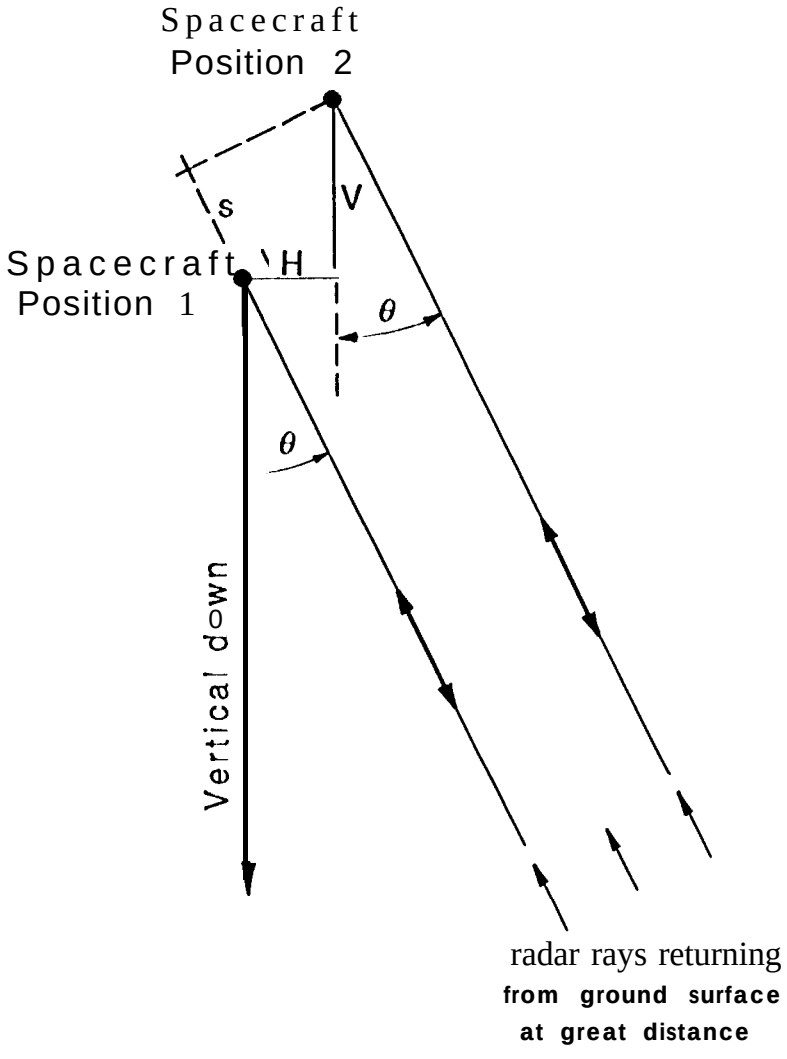

FIG. 2

GOLDSTEIN ET AL.

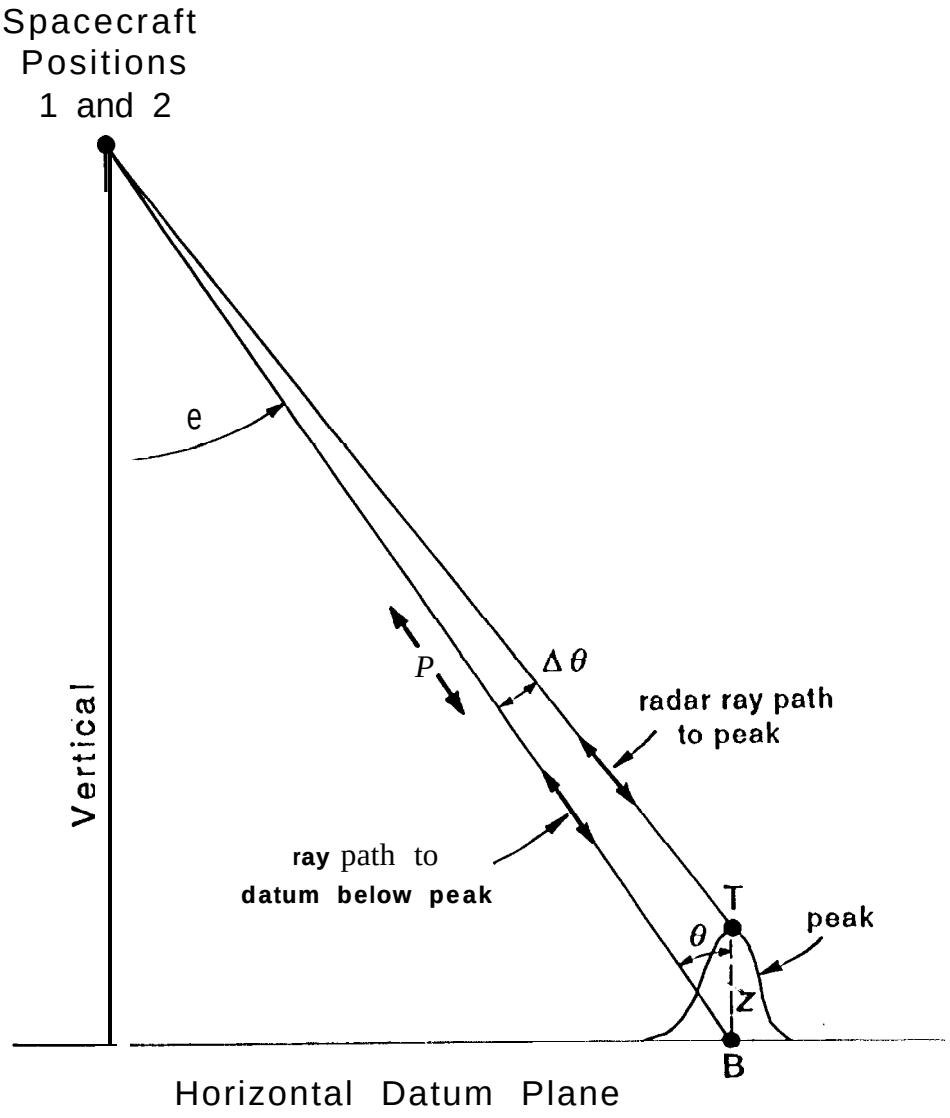

FIG. 3

Goldstein et al.

Fig. 3

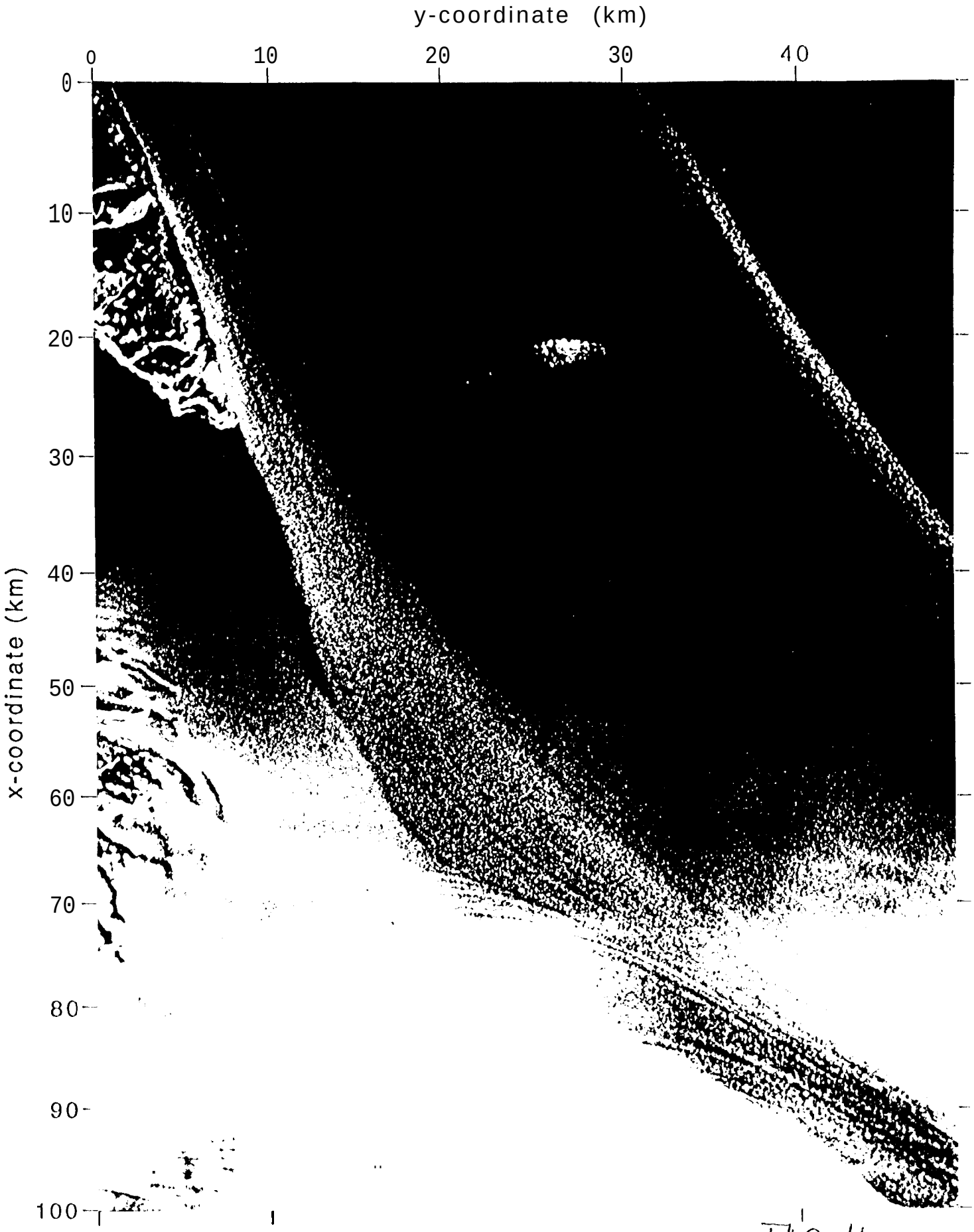

FIG. 4
Goldstein et al.

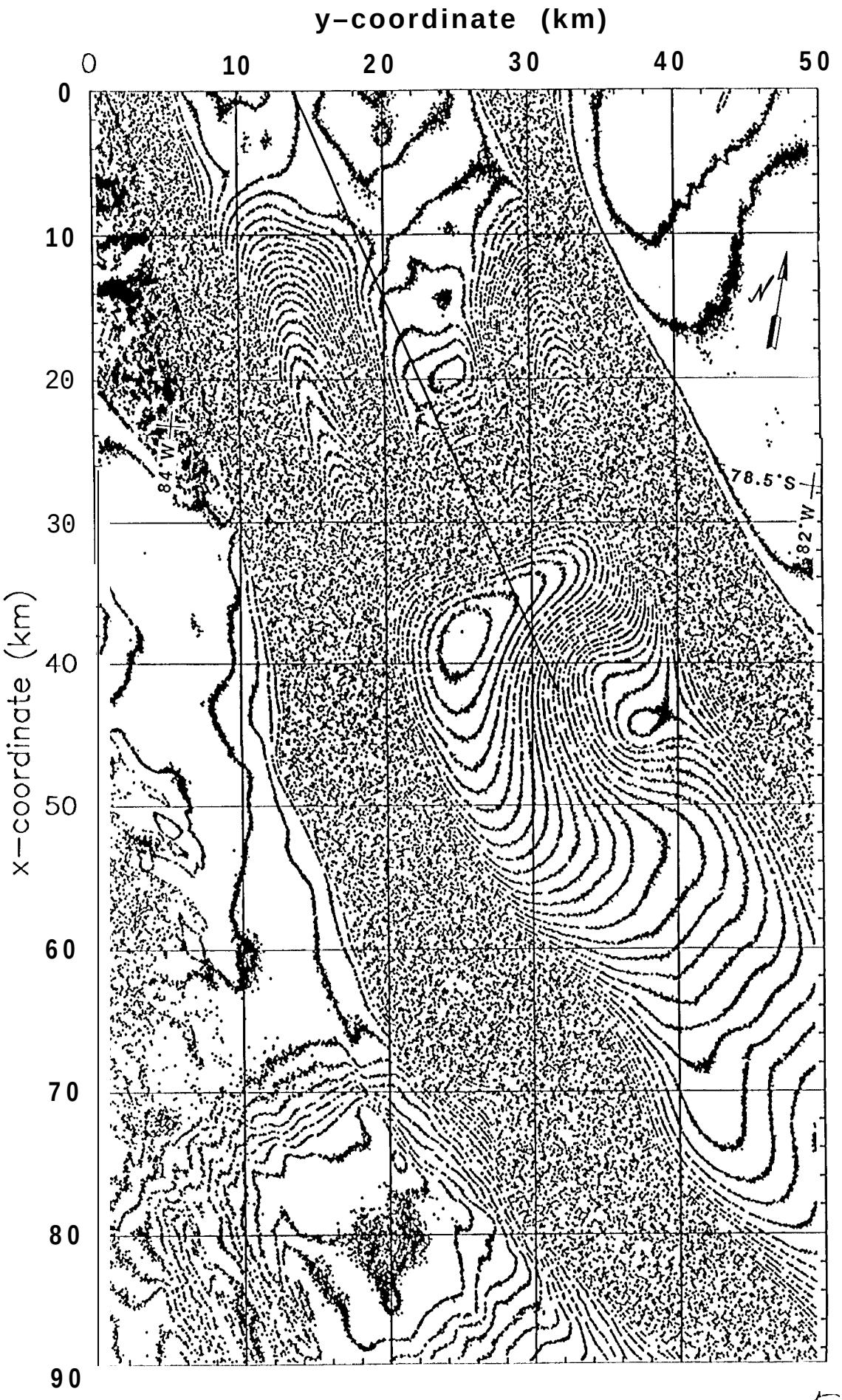

F16.5

Goldstein et al.

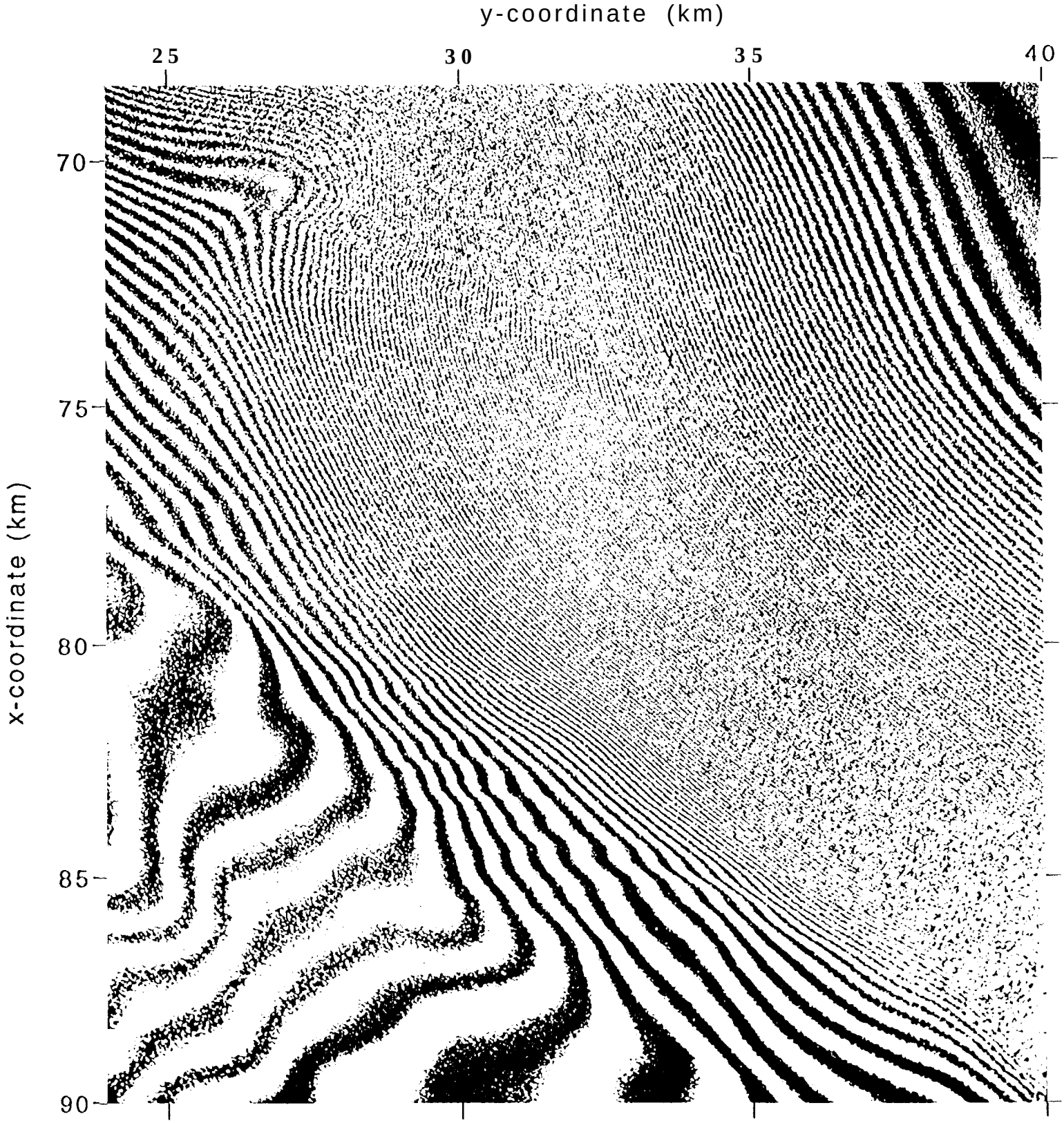

FIG. 6

Goldstein et a

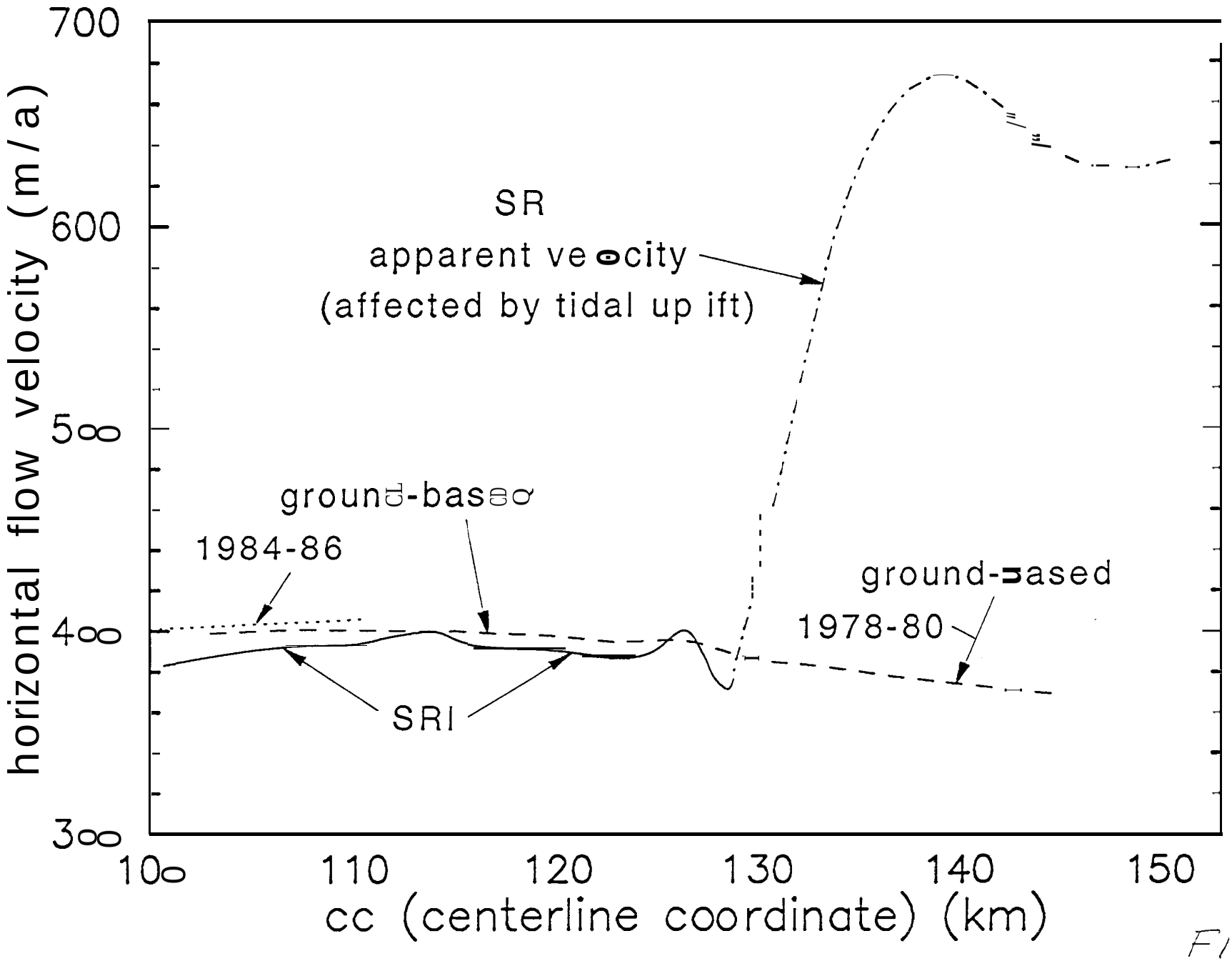

FIG 7
Goldstein et al.

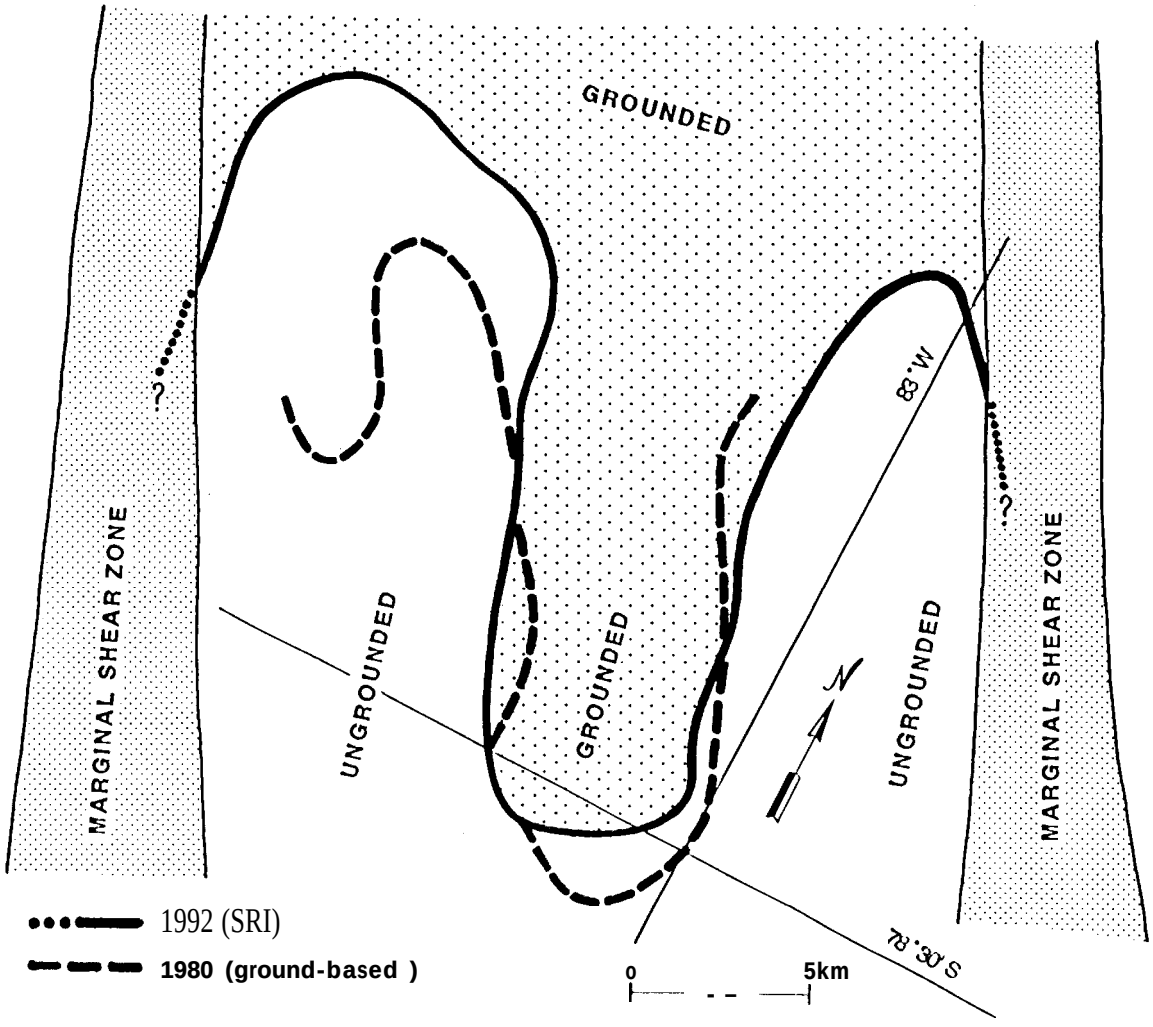

FIG. 9

Goldstein et al.

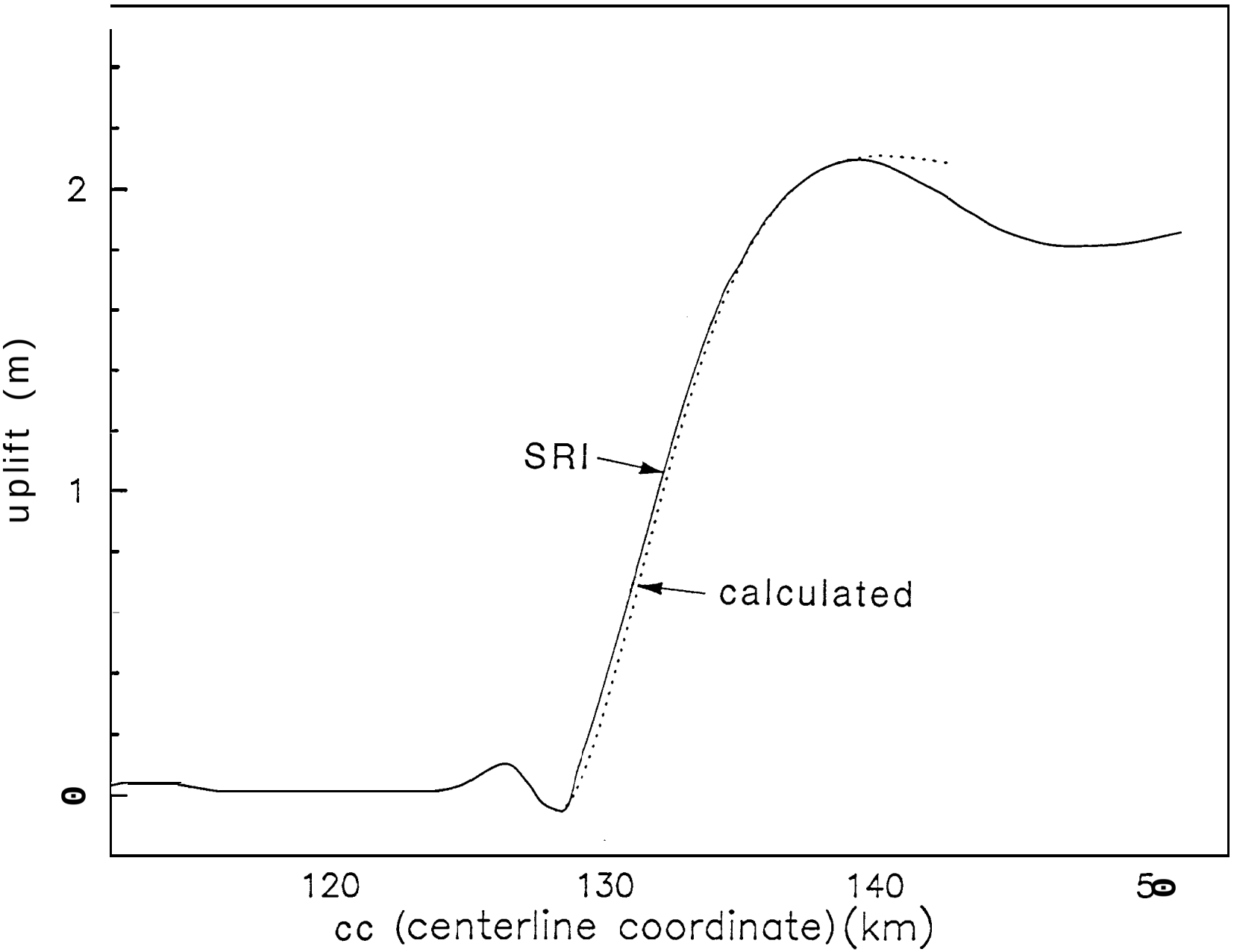
uplift (m)
2
1
0
SRI
calculated
120
130
140
cc (centerline coordinate)(km)

FIG. 10.